Journal of Nuclear Materials 459 (2015) 114–121

Contents lists available at ScienceDirect

Journal of Nuclear Materials

journal homepage: www.elsevier.com/locate/jnucmat

Separation of actinides from irradiated An–Zr based fuel by electrorefining on solid aluminium cathodes in molten LiCl–KCl

P. Souček [a,*], T. Murakami [b], B. Claux [a], R. Meier [a], R. Malmbeck [a], T. Tsukada [b], J.-P. Glatz [a]

[a] European Commission, Joint Research Centre (JRC), Institute for Transuranium Elements (ITU), Postfach 2340, 76125 Karlsruhe, Germany
[b] Central Research Institute of Electric Power Industry (CRIEPI), Komae-shi, Tokyo 201-8511, Japan

HIGHLIGHTS

- Electrorefining process in molten LiCl-KCl using solid Al electrodes was demonstrated.
- High separation factors of actinides over lanthanides were achieved.
- Efficient recovery of actinides from irradiated nuclear fuel was achieved.
- Uniform, dense and well adhered deposits were obtained and characterised.
- Kinetic parameters of actinide–aluminium alloy formation were evaluated.

ARTICLE INFO

Article history:
Received 25 September 2014
Accepted 19 December 2014
Available online 10 January 2015

ABSTRACT

An electrorefining process for metallic spent nuclear fuel treatment is being investigated in ITU. Solid aluminium cathodes are used for homogeneous recovery of all actinides within the process carried out in molten LiCl–KCl eutectic salt at a temperature of 500 °C. As the selectivity, efficiency and performance of solid Al has been already shown using un-irradiated An–Zr alloy based test fuels, the present work was focused on laboratory-scale demonstration of the process using irradiated METAPHIX-1 fuel composed of U_{67}–Pu_{19}–Zr_{10}–MA_2–RE_2 (wt.%, MA = Np, Am, Cm, RE = Nd, Ce, Gd, Y). Different electrorefining techniques, conditions and cathode geometries were used during the experiment yielding evaluation of separation factors, kinetic parameters of actinide–aluminium alloy formation, process efficiency and macro-structure characterisation of the deposits. The results confirmed an excellent separation and very high efficiency of the electrorefining process using solid Al cathodes.

1. Introduction

The electrorefining process for treatment of spent nuclear fuel in molten chloride salts is being investigated since 1950s, when this method for recovery of actinides from the Experimental Breeder Reactor II (EBR-II) spent fuel was proposed by the Argonne National Laboratory (ANL) [1]. This research led eventually to the development of the Integral Fast Reactor (IFR) concept in mid-1980s, which included on-site processing and recycling of discharged core and blanket fuel materials from EBR-II by electrorefining in a molten LiCl–KCl based electrolyte [2]. Although more than four metric tons of spent fuel were treated by the pyroprocess at ANL, only U was recovered on solid inert cathode and tests to recover U together with Pu and MA on reactive liquid cathode were carried out.

Nowadays, one of the most important aim of the developed advanced nuclear energy systems [3] is the recycling of all actinides in order to reduce the amount and radiotoxicity of the spent fuel and also to utilise effectively the resources. Minimisation of the generated nuclear waste is also the goal of Partitioning & Transmutation (P&T) strategies, which aim at reducing the long-term radiotoxicity of spent fuel by transmuting plutonium, minor actinides (Np, Am, Cm), and long lived fission products (Cs, Sr) in dedicated reactors [4,5].

A pyrochemical process for the grouped recovery of all actinides from spent metallic fuel has been proposed by ITU [6]. It is based on electrorefining in molten LiCl–KCl eutectic mixture using solid reactive aluminium cathodes [7]. The fuel is chopped, loaded into a tantalum basket, immersed into the salt and electrochemically dissolved. Actinides, alkali, alkaline earth metal and rare earth fission products (FP) are dissolved into the melt during the process, but due to a controlled deposition potential, only actinides are group-selectively electrodeposited on solid aluminium cathodes as solid actinide–aluminium (An–Al) alloys. The electrorefining

* Corresponding author. Tel.: +49 (0) 7247 951124; fax: +49 (0) 7247 951588.
E-mail address: Pavel.Soucek@ec.europa.eu (P. Souček).

http://dx.doi.org/10.1016/j.jnucmat.2014.12.103
0022-3115/

can be controlled in order to prevent oxidation of zirconium and noble metal FPs, but in the real process, their co-oxidation is expected in correlation with the required portion of recovered actinides and used current [8,9].

In ITU, the electrorefining process has been tested using metallic experimental METAPHIX-1 fuel composed of U_{61}–Pu_{22}–$Am_{2.0}$–$Nd_{3.5}$–$Gd_{0.5}$–$Y_{0.5}$–$Ce_{0.5}$–Zr_{10}, which was synthesised in ITU in collaboration with Central Research Institute of Electric Power Industry (CRIEPI, Japan) [10]. An excellent recovery of An over lanthanides and high efficiency of the process has been demonstrated by processing the un-irradiated fuel [11,12]. A very high capacity of solid aluminium to take-up actinides has been shown by dedicated electrorefining experiments using U–Pu–Zr alloy [13,14].

The present work describes a study of the electrorefining process using solid aluminium cathodes processing METAPHIX fuel irradiated in the PHENIX reactor. The details of the irradiation and the fuel characterisation before and after irradiation have been published in [15]. Part of the pin 2 of METAPHIX-1 fuel with an initial composition U_{67}–Pu_{19}–Zr_{10}–MA_2–RE_2 (wt.%, MA = Np, Am, Cm, RE = Nd, Ce, Gd, Y) and a burn-up of 2.5 at.% was used. The experiments were mainly focused on determination of the actinides separation factors and characterisation of the deposits in dependency on the used current density. An evaluation of the kinetic parameters of the actinide–aluminium formation was also done.

2. Experimental

All experiments and storage and handling of chemicals were carried out in a biological shielded hot cell under purified Ar atmosphere (<10 ppm of water and oxygen). The cell is equipped with a vertical furnace and stainless steel electrolyser described in detail in [16]. About 130 g of LiCl–KCl eutectic melt already containing 5.64 wt.% actinides and 0.22 wt.% lanthanides from previous experiments was used as electrolyte, the exact composition and concentration development is described below in Section 3.6, Table 9. An alumina crucible served as a container for the melt. The operating temperature was 500 °C.

The electrorefining runs were carried out with a three electrodes set-up using cathodes from aluminium plates with dimensions 0.3 × 0.1 cm and rods with diameter 0.3 cm dipped into the melt for 1.1–1.5 cm, whilst the exact immersion depth was measured after each run. The electrorefined material was loaded in a stainless steel basket connected as anode. Both anode and cathode potentials were measured using a reference electrode based on U^{3+}/U couple, which was prepared before each experiment by a short electrodeposition of U metal on a W wire.

The main series of runs (1–7) was done galvanostatically using 3.176 g of the METAPHIX-1 irradiated fuel. In addition, a series of potentiostatic runs (8–11) was carried out with pure uranium metal dendrites obtained from the previous experiments. All galvanostatic runs (except run 1 and 7, see detailed explanation in Section 3.1) were stopped when the maximum possible amount of An, in the form of An–Al alloys, had been deposited on the electrode surface avoiding formation of U metal. The kinetic properties of An in solid Al were estimated from the dependency of the An–Al alloy layer thickness on the time of the electrodeposition.

During all runs, salt and deposit samples were taken for inductively coupled plasma mass spectrometry (ICP-MS) analysis. Salt samples were directly dissolved in 1 M HNO_3, whilst deposit samples were first washed with water to remove the adhered salt and then immersed in concentrated HNO_3, which dissolved only the An–Al layer. Pure Al residues settled down in the dissolution tube and only the clear solutions were sampled and analysed. These results were used to evaluate the separation factors for each element in order to show the selectivity of the process.

3. Results and discussion

3.1. Galvanostatic electrorefining runs

Altogether, 7 runs using Al plate (1–5) and rod (6–7) cathodes were carried out using different constant current densities in a range of 10–40 mA cm^{-2}. The runs were stopped after reaching the uranium metal deposition potential with two exceptions. In run 1, the potential quickly dropped below this limit, but the experiment was continued to evaluate the influence of formation of uranium dendrites on the deposit morphology. Run 7 was stopped when the anode potential got too close to the Zr dissolution potential. All galvanostatic runs are described in Table 1, where the normalised current density (j_{norm}) is the current density (j) divided by the total concentration of actinides in the melt and 'loading' is the expected used-up capacity of the immersed part of the cathode, estimated for the formation of $AnAl_3$ alloy from all deposited An (calculated for uranium) according to the passed charge (Q). The evolutions of the cathode potentials are shown separately for the plate and rod electrodes in Figs. 1 and 2.

An example of the anodic potential evolution for run 7, which had to be stopped to prevent Zr dissolution to the melt, is shown

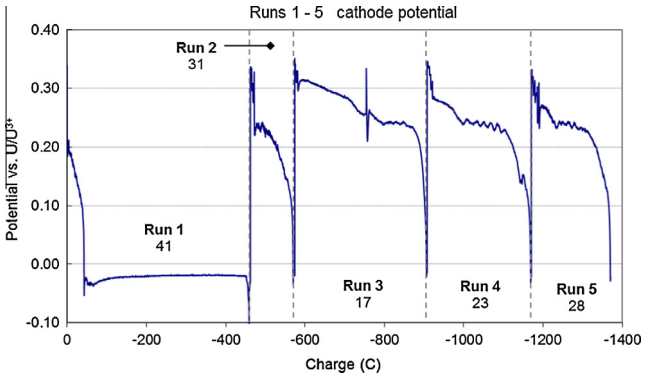

Fig. 1. Cathodic potential developments during galvanostatic runs 1–5 using Al plates with the current densities indicated as numbers below the run labels.

Table 1
Summary of the galvanostatic runs. Run 1–5: plate cathodes; runs 6–7: rod cathodes.

Run	i (mA)	j (mA/cm^2)	$j_{norm.}$ (mA/cm^2/wt.% An)	Q (C)	Loading (%/UAl_3)
1	50	40.7	7.2	43/459*	10.0/106.1*
2	28	30.8	5.1	115	36.0
3	18	16.8	2.9	335	89.0
4	23	23.2	4.1	263	76.0
5	28	28.3	5.0	250	58.0
6	22–20	18.3–16.6	3.3–3.0	464	56.9
7	12	10.8	1.8	637	85.2

* In run 1, the numbers X/Y representing values achieved before reaching the U metal deposition potential (X) and a sum value of the complete run (Y).

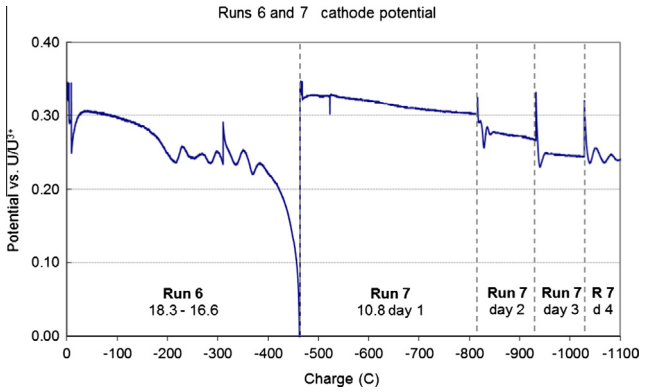

Fig. 2. Cathodic potential developments during galvanostatic runs 6–7 using Al rods with the current densities/days of the runs indicated as numbers below the run labels.

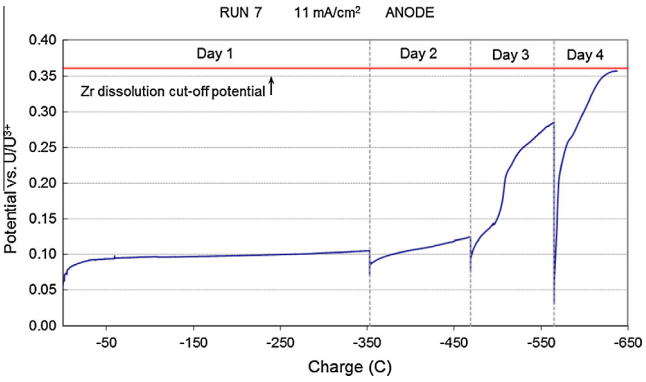

Fig. 3. Anodic potential during galvanostatic run 7.

Table 2
Summary of the potentiostatic runs 8–11 using Al plate cathodes.

Run	E (V vs. U/U^{3+})	t (s)	Q (C)	L (mm)	Loading (%/UAl_3)
8	+0.11 (=−1.26 V vs. Ag/Ag^+)	5676	179.2	0.45	56.5
9		2914	126.8	0.36	40.0
10		8500	250.7	0.58	79.0
11		1500	62.7	0.21	19.8

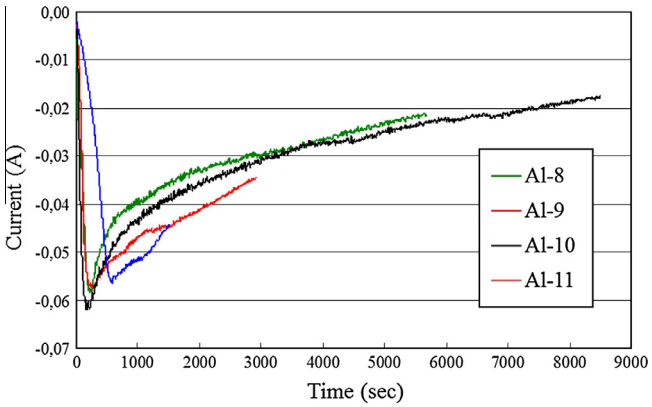

Fig. 4. Current developments for the potentiostatic electrorefining runs 8–11.

in Fig. 3. The potential corresponding to the start of Zr oxidation was estimated based on polarisation curves measured using pure Zr metal in the melt used for the experiment. Its value 0.36 V vs. U/U^{3+} is in a good agreement with the typically used anodic cut-off potential for Zr, i.e., −1.00 V vs. Ag/Ag^+, since the relation between both reference potentials during the present experiment was derived to be $E(Ag/Ag^+) = 1.36\ V + E(U/U^{3+})$. Based on the mass balance calculations, approximately 72% of actinides were dissolved from the fuel before the Zr cut-off potential was reached.

3.2. Potentiostatic electrorefining runs

Four potentiostatic runs (8–11) were carried out using Al plate cathodes (1 × 3 × 11 mm) with the main aim of evaluating the transport properties of An into solid Al. In addition, since the runs were carried out with the minor actinides and lanthanides containing salt from the previous METAPHIX-1 electrorefining (however not directly after run 7), the deposits were also used for evaluation of the separation factors of actinides and lanthanides. The runs are characterised in Table 2. All runs were carried out at a potential (E) of +0.11 V vs. U/UCl_3 to prevent the lanthanides co-deposition and various electrolysis durations were applied to be able to evaluate the dependency of the alloy layer thickness (L) on the deposition time (t).

Fig. 4 shows the current evolutions during the potentiostatic runs. At the initial stages of all runs, the cathodic current increased mainly due to the increase of the effective electrode surface area increase with the Al–An alloy formation. Then a gradual decrease of the cathodic current followed, as the alloy formation become more difficult with the increase of the alloy layer.

3.3. Characterisation of deposits

All electrodes were left above the melt after the experiment for several hours to let the adhered salt drop off, but they were not washed. After weighting they were transversely cut at half-height of the immersed parts and the cuts were observed by optical microscopy. For each electrode, one half of the deposit was analysed by ICP-MS, the other kept for further experimental purposes. In all cases, a uniform, dense and well adhered metallic-shiny deposit was obtained as shown in Figs. 5–7. Run 1 represents a special case, as the potential was under U metal deposition during most of the run and metallic uranium was allowed to deposit up to the complete saturation of the electrode. It was found that the deposited U metal reacted very rapidly with Al, forming U–Al alloy, as the aluminium was fully loaded with U. Only after consumption of all Al, U dendrites were formed on the alloy surface, as visible in Fig. 5. However, this situation is not expected in the real process, as the cathodic potential will be likely controlled in a way to avoid co-deposition of lanthanides as Ln–Al alloys, which occurs at slightly more positive potential than U metal deposition, depending on the lanthanides concentration.

From the ICP-MS elemental analyses of all deposits, the molar ratio of Al–An (sum of U, Pu, Np, Am and Cm) was calculated. They are plotted in Fig. 8 against the specific charge, defined as the passed charge divided by electrode surface area. It shows that most of the deposits were composed of $An–Al_3$ alloys, but the molar ratio changes from 3 to 4 if the specific charge is decreased, which corresponds to lower loading of Al.

In addition, the masses of the deposits were estimated from the analyses of the cut parts for all runs except run 1 (dendrites formation) and run 7 (inhomogeneous deposit) under assumption of uniform An–Al alloy formation on the electrode surface and knowing the dimensions of the complete deposits. The masses of the deposits directly after the runs, i.e., including the adhered salt (m_{exp}), are summarised in Table 3 together with the estimated salt

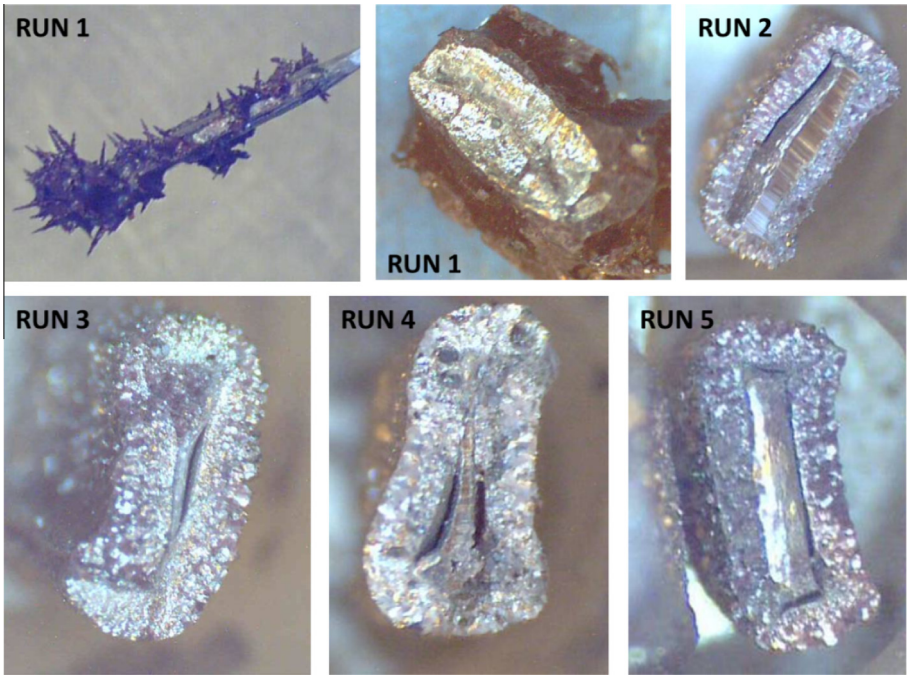

Fig. 5. Optical microscopy photographs of the transverse cuts of the Al cathodes after galvanostatic runs 1–5.

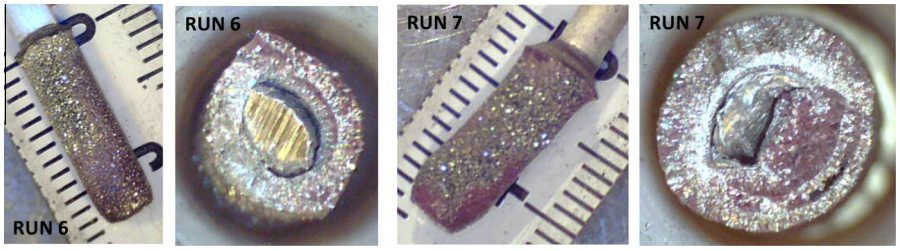

Fig. 6. Optical microscopy photographs of the Al cathodes and their transverse cuts after galvanostatic runs 6–7.

content and the masses evaluated from the elemental analyses ($m_{\text{ICP-MS}}$). The theoretical mass (m_{th}) was calculated from Faraday's law using molar mass of uranium as the main expected constituent of the deposit.

3.4. Kinetic properties of An in solid Al

The thicknesses of the alloy layers were measured at comparable heights of the electrodes from runs 2–5 and 8–11 using the optical microscopy photographs of the transverse cuts of the electrodes. As expected, at lower current density the slower deposition rate allowed formation of thicker An–Al alloy surface layer before deposition of U metal than at high current density. The dependency of the final thickness of the An–Al alloy layer (L) on the current density was linear (see Fig. 9 left). The current density was determined as an average of the values for initial and final surfaces of the electrodes. In addition, a linear relationship between square of L and electrolysis time (t) was shown for the potentiostatic runs

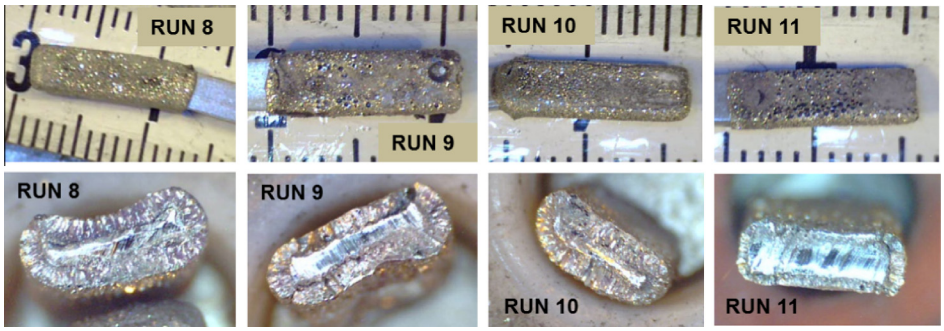

Fig. 7. Optical microscopy photographs of the Al cathodes and their transverse cuts after potentiostatic runs 8–11.

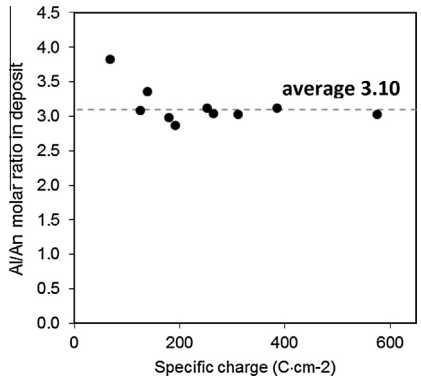

Fig. 8. Molar ratio of Al–An in the deposits from runs 2–10 plotted against the specific charge.

(see Fig. 9 right). This indicates that the diffusion in the alloy layer is the rate determining step of the alloy layer formation, which is therefore governed by the parabolic law according to equation (1):

$$L^2 = K_p \cdot t \quad (1)$$

The parabolic law constant (K_p) was evaluated from the gradient of the regression line of the L^2 on t dependency for potentiostatic runs to be $3.9 \cdot 10^{-7}$ cm^2 s^{-1}. The exact calculation of the diffusion coefficient of An in solid Al is not possible from the present experiment, as achievement of the necessary conditions cannot be proven. The correct evaluation requires a homogeneous potential on the complete electrode surface, yielding constant activity of the deposited metal in the formed alloy and formation of one-phase alloy with known composition. Nevertheless, the value of the diffusion coefficient can be expected in the same order of magnitude as the parabolic law constant. This value is similar to the published diffusion coefficients for the comparable systems of rare earths – Ni solid alloys (about 10^{-6} cm^2 s^{-1}) [17].

Table 4
Relative content of An and Ln in the deposits from runs 1–7.

Run	1	2	3	4	5	6	7
U	72.13	92.92	98.05	96.16	95.36	97.78	99.39
Np	0.62	0.36	0.13	0.23	0.28	0.15	0.06
Pu	26.97	6.70	1.82	3.60	4.34	2.05	0.55
Am	0.14	0.02	0.00	0.01	0.01	0.01	0.00
Cm	0.03	0.00	0.00	0.00	0.00	0.00	0.00
Sum An	99.89	99.99	100.00	100.00	100.00	100.00	99.99
Sum Ln	0.11	0.01	0.00	0.00	0.00	0.00	0.01

Table 5
Separation factors normalised to uranium for galvanostatic runs 1–7.

Run	1	2	3	4	5	6	7
j (mA cm^{-2})	−41	−31	−17	−23	−28	−17	−11
U	1	1	1	1	1	1	1
Np	2.55	7.43	23.8	12.9	10.4	19.1	62.4
Pu	3.29	20.3	78.8	39.6	31.8	65.9	274
Am	5.25	58.2	277	105	82	211	916
Cm	9.29	132	703	303	254	521	1930
La	386	8080	8347	2100	4111	3646	2078
Ce	84.5	2407	8507	2642	4276	4156	2001
Pr	68.7	1665	7098	2963	2669	3672	2005
Nd	55.4	1483	7692	2982	3432	3839	2013
Pm	225	4438	7927	3193	4888	3311	2063
Sm	303	5358	10,402	3201	7371	3316	1857
Eu	405	8529	10,849	3448	7449	3072	1520
Gd	70.3	1574	7309	3283	3644	3289	1864
Tb	62.2	1940	7059	3431	3328	3043	1736
Dy	66.7	1764	8419	3366	3499	3347	2447
Y	274	4618	9684	4352	5612	3365	1776

3.5. Separation factors

The separation factors SF_M were calculated as the concentration ratio of the given element M in the salt ($X_{M\ in\ salt}$) and in the deposit ($X_{M\ in\ Al}$). For better comparison, the SF_M were related to the values of U, according to the equation (2):

Table 3
Mass balance of the deposit.

Run	1	2	3	4	5	6	7	8	9	10	11
$m_{th.}$	0.379	0.095	0.277	0.217	0.165	0.383	0.526	0.148	0.105	0.207	0.052
$m_{exp.}$	0.504	0.119	0.339	0.263	0.214	0.504	0.683	0.182	0.126	0.244	0.066
% of salt	24.8	20.2	18.3	17.5	22.7	24.0	23.0	18.7	16.7	15.2	21.2
m_{ICP-MS}	n/a	0.079	0.263	0.186	0.141	0.359	n/a	0.143	0.088	0.190	0.047

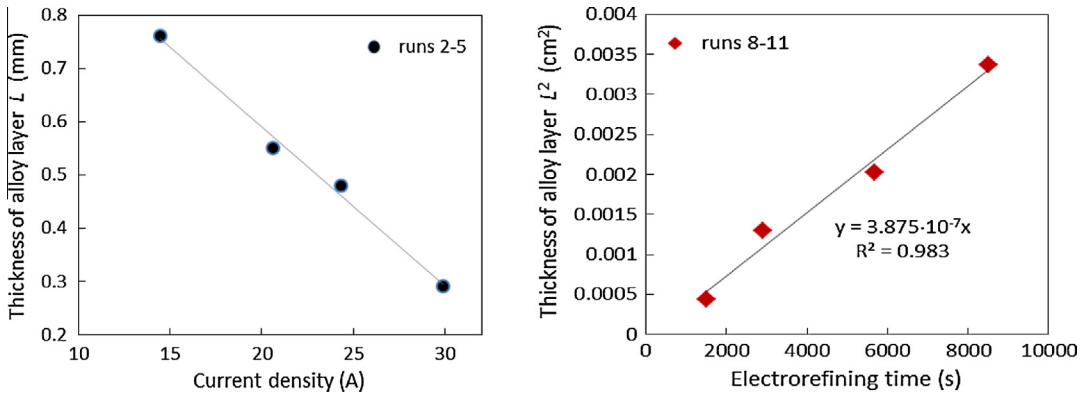

Fig. 9. Left – dependency of the thickness of the An–Al alloy layers on current density. Right – dependency of the square of the alloy layer thickness and electrolysis time.

Table 6
Relative content of An and Ln in the deposits from runs 8–11.

Run	8	9	10	11
U	70.86	80.20	74.08	79.74
Np	1.05	0.75	0.87	0.71
Pu	28.02	18.99	24.97	19.48
Am	0.06	0.05	0.07	0.06
Cm	0.01	0.01	0.01	0.01
Sum An	99.99	100.00	99.99	100.00
Sum Ln	0.01	0.00	0.01	0.00

Table 7
Separation factors normalised to U for potentiostatic runs 8–11.

Run	8	9	10	11
Potential	−1.26 V vs. Ag/AgCl			
U	1	1	1	1
Np	2.45	3.85	2.95	3.86
Pu	4.67	7.79	5.30	7.32
Am	17.3	25.3	14.8	20.5
Cm	60.4	83.2	47.3	61.4
La	1879	9294	5109	7432
Ce	3620	6612	4356	6525
Pr	1141	2800	1799	2917
Nd	1820	4008	2152	3610
Pm	1649	3394	1632	2409
Sm	2242	3008	1730	3718
Eu	2427	2903	1495	3623
Gd	2234	2932	1501	2564
Tb	2183	3071	1303	2124
Dy	2572	3191	1666	2104
Y	2145	2641	1666	2610

$$SF_M = (X_{M\ in\ salt}/X_{M\ in\ Al})/(X_{U\ in\ salt}/X_{U\ in\ Al}) \quad (2)$$

In addition, the relative contents of actinides in the deposits were calculated for each run to demonstrate selectivity of the process. The results are summarised in Tables 4–7.

For illustration, the dependence of the separation factors on the current density is shown also in Fig. 10, separately for actinides and lanthanides. It was found that the separation factor of actinides increased with decrease of the current density. Although the data are significantly more scattered for lanthanides, their separation factors seem to have a similar trend, as expected.

3.6. Current efficiency and concentration profile

The current efficiencies summarised in Table 8 were calculated under the same assumptions as discussed in Section 3.3 for the estimation of masses of the complete deposits. The calculation was based on comparison of the passed charge with the charge theoretically needed to deposit the amount of all elements analysed in the deposit according to Eq. (3), where m is the mass of each element as analysed by ICP-MS in the deposit [g], M is molar mass of the element, F is Faradays constant, z is the number of exchanged electrons and Q_p is the total charge passed in each run [C].

$$R = \sum \left(\frac{m}{M} Fz\right)/Q_p \quad (3)$$

In addition, the concentration profile of the most important elements contained in the melt during the experiment in dependency of the sum of the passed charge is shown in Fig. 11, evaluated from the ICP-MS analyses of the salt samples. The melt was used for a different experiment in between the galvanostatic and potentiostatic runs, thus the concentration changed and the profiles for both series are presented separately. Each point corresponds to one sample, taken at the end of each run (runs 1–7) or each second run (runs 8–11). Although, the U concentration should typically decrease and the Pu content increase [14], this effect was not observed in this case, probably due to the relatively high absolute masses of these elements dissolved in the initial salt in comparison to the masses deposited during the experiment. The analysed sharp drop of uranium concentration in the melt between runs 1 and 2 was not expected and it does not correspond to both theoretically and really deposited mass of uranium during run 2. The discrepancy originated probably due to analysis technical problem or cross-contamination of the initial samples during technically very demanding preparation in hot cells. The overall concentration of

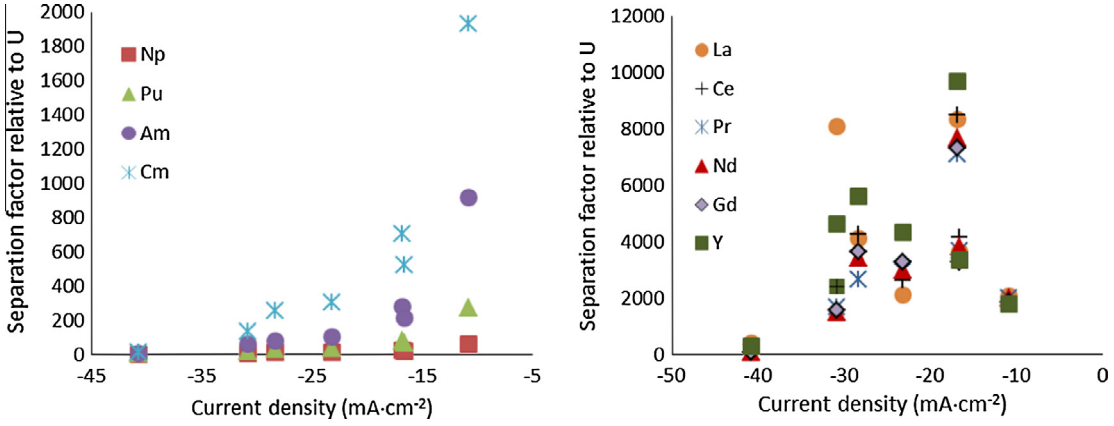

Fig. 10. Dependence of the normalised separation factors of actinides (left) and lanthanides (right) on the applied current density.

Table 8
Current efficiencies for galvanostatic runs 2–6 and potentiostatic runs 8–11.

Run	2	3	4	5	6	8	9	10	11
Current density ([mA cm^{-2}]/potential)	−31	−17	−23	−28	−17	−1.26 V vs. Ag/AgCl			
Current efficiency R (%)	83.9	95.5	86.1	89.6	94.1	97.2	85.0	92.4	91.5

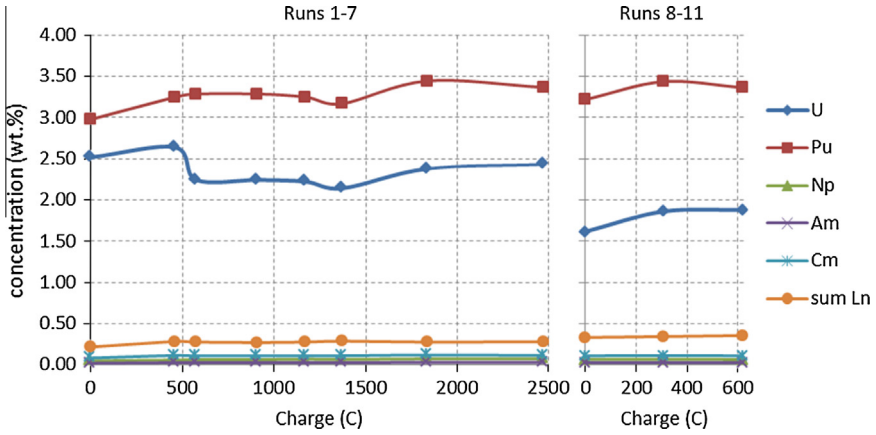

Fig. 11. Concentration profile in the melt during the experiment.

Table 9
Composition of the melt at the beginning (c_i) and end (c_f) of the galvanostatic series (wt.%).

	U	Np	Pu	Am	Cm	La	Ce	Pr	Nd	Pm	Sm	Gd	Y
c_i	2.52	0.05	2.98	0.02	0.08	0.02	0.05	0.01	0.10	0.00	0.01	0.01	0.01
c_f	2.43	0.07	3.36	0.03	0.11	0.02	0.07	0.02	0.13	0.01	0.01	0.02	0.01

lanthanides remained constant, as expected. The initial and final compositions of the melt for the galvanostatic runs 1–7 are summarised in Table 9.

4. Conclusion

Electrorefining of irradiated metallic test fuel METAPHIX-1 with initial composition of 2 wt.% minor actinides (Np, Am, Cm) and 2 wt.% rare earths (Nd, Ce, Gd, Y) has been carried out with the aim to demonstrate the group-selective homogeneous recovery of all actinides using solid aluminium cathodes. The results have demonstrated an excellent performance of this cathodic material, as a very efficient separation between An and Ln has been achieved at all studied current densities, which is fully in agreement with the previous studies on un-irradiated fuel. Recovery of uranium has been accomplished with high efficiency, whilst Pu and minor actinides have been partly co-deposited and partly accumulated in the melt. The applied cathodic cut-off potential was set to −1.48 V vs. Ag/AgCl corresponding to U metal deposition, and not to a more positive potential corresponding to start of lanthanide-aluminium alloys formation, i.e., −1.35 V vs. Ag/AgCl for Nd–Al alloy (both values are apparent standard potentials taken from [18]). In spite of this fact, the deposits contained only traces of lanthanides. Even in the run 1, in which a charge of 416 C was passed slightly more negative than the U metal deposition potential, the deposit was composed of 99.89% of actinides. The evaluated separation factors normalised to the value of U were in a range of 10^3–10^4 for the rare earths.

Uniform, dense, homogeneously distributed and well adhered deposits composed predominantly of $AnAl_3$ alloys were obtained, independent on the geometry of the cathodes and without rotating them. A dependency on the maximum thickness of the An–Al alloy layer formed on the electrode surface without reduction of U metal on the current density has been determined, which is an important parameter for scale-up engineering studies of the process. Generally, the maximum achievable alloy layer thicknesses are relatively low, e.g., for a current density of 20 mA cm^{-2} it is only 0.55 mm. It indicates a necessity of using large surface thin cathodes in the larger scale process.

In addition, it has been shown that the diffusion in the alloy layer is the rate determining step of the alloy layer formation, governed by the parabolic law. The parabolic law constant has been evaluated to be in a range of 10^{-7} cm^2 s^{-1}. It indicates that the diffusion coefficient of actinides in the solid Al–An alloy can likely be in the same order of magnitude; however the exact calculation is principally not possible from the present experiment.

Although the basic factors of the studied electrorefining process has been demonstrated, further developments will be needed, still in a laboratory scale. It should be focused mainly on the selectivity limits under conditions simulating the final stages of the process, i.e., involving significantly higher concentration of lanthanides in the electrolyte. The behaviour and distribution of Zr and noble metals in dependency on the portion of recovered actinides from the irradiated fuel should be also studied with the aim to optimise the process parameters.

Acknowledgements

The authors wish to thank B. Lynch and S.V. Winckel for ICP-MS analyses and A. Rodrigues and M. Ougier for experimental support. This work was carried out with the European Commission financial support in the 7th framework program, under the collaborative project "SACSESS", Grant Agreement No. 323282.

References

[1] M.A. Williamson, J.L. Willit, Nucl. Eng. Technol. 43 (4) (2011) 329–334.
[2] J.J. Laidler, J.E. Battles, W.E. Miller, J.P. Ackerman, E.L. Carls, Prog. Nucl. Energy 31 (1–2) (1997) 131–140.
[3] U.S. DOE Nuclear Energy Research Advisory Committee at the Generation IV International Forum (December 2002, GIF-002-00), 2002, <http://www.gen-4.org/PDFs/GenIVRoadmap.pdf>.
[4] J. Magill, V. Berthou, D. Haas, J. Galy, R. Schenkel, H.-W. Wiese, G. Heusener, J. Tommasi, G. Youinou, Nucl. Energy 42 (5) (2003) 263–277.
[5] Implications of Partitioning and Transmutation in Radioactive Waste Management, in Technical Report Series No. 435. 2004, International Atomic Energy Agency, Vienna, Austria, STI/DOC/010/435, ISSN 0074-1914, ISBN 92-0-115104-7.
[6] P. Souček, R. Malmbeck, C. Nourry, J.P. Glatz, Energy Proc. 7 (2011) 396–404.
[7] J. Serp, M. Allibert, A. Le Terrier, R. Malmbeck, M. Ougier, J. Rebizant, J.-P. Glatz, J. Electrochem. Soc. 152 (3) (2005) C167–C172.

[8] B.R. Westphal, D. Vaden, S.X. Li, G.L. Fredrickson, R.D. Mariani, Fate of noble metals during the pyroprocessing of spent nuclear fuel, in: Proceedings of Global 2009, Paper 9309, September 6–11, Paris, France, 2009, pp. 1291–1297.
[9] R.K. Ahluwalia, T.Q. Hua, H.K. Geyer, Nucl. Technol. 133 (1) (2001) 103–118.
[10] H. Ohta, T. Ogata, D. Papaioannou, M. Kurata, T. Koyama, J.-P. Glatz, V.V. Rondinella, J. Nucl. Sci. Technol. 48 (4) (2011) 654–661.
[11] O. Conocar, N. Douyere, J.-P. Glatz, J. Lacquement, R. Malmbeck, J. Serp, Nucl. Sci. Eng. 153 (2006) 253–261.
[12] P. Souček, R. Malmbeck, E. Mendes, C. Nourry, J.-P. Glatz, Recovery of actinides from spent nuclear fuel by pyrochemical reprocessing, in: Proceedings of Global 2009, Paper 9217, September 6–11, Paris, France, 2009, pp. 1156–1165.
[13] L. Cassayre, R. Malmbeck, P. Masset, J. Rebizant, J. Serp, P. Soucek, J.P. Glatz, J. Nucl. Mater. 360 (1) (2007) 49–57.
[14] P. Souček, L. Cassayre, R. Malmbeck, E. Mendes, R. Jardin, J.-P. Glatz, Radiochim. Acta 96 (2008) 315–322.
[15] H. Ohta, T. Ogata, T. Yokoo, M. Ougier, J.P. Glatz, B. Fontaine, L. Breton, Nucl. Technol. 165 (1) (2009) 96–110.
[16] T. Kato, T. Murakami, K. Uozumi, T. Koyama, M. Ougier, A. Rodrigues, S. van Winkel, R. Malmbeck, J.-P. Glatz, Actinides recovery from irradiated MOX fuel by pyrochemical reprocessing, in: Proceedings of Proceedings of Global 2011, Paper No. 391320, Makuhari, Japan, December 11–16, 2011.
[17] P. Taxil, P. Chamelot, L. Massot, C. Hamel, J. Mining Metall. 39 (1–2B) (2003) 177–200.
[18] J.-P. Glatz, R. Malmbeck, P. Souček, B. Claux, R. Meier, M. Ougier, T. Murakami, Development of pyrochemical separation processes for recovery of actinides from spent nuclear fuel in molten LiCl–KCl, in: F. Lantelme, H. Groult (Eds.), Molten Salts Chemistry, Elsevier, Oxford, 2013, pp. 541–560.